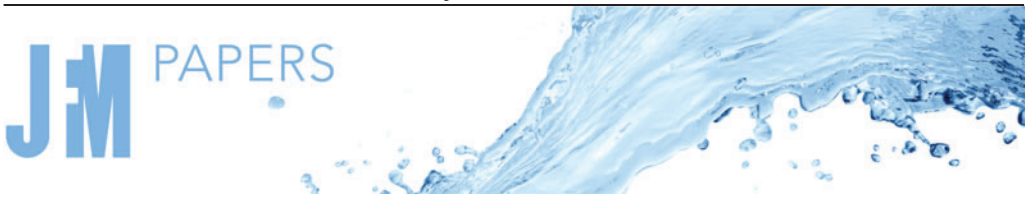
J. Fluid Mech. (2023), *vol*. 975, A1, doi:10.1017/jfm.2023.686



Scattering of swell by currents

Han Wang[1],†, **Ana B. Villas Bôas**[2], **William R. Young**[3] **and Jacques Vanneste**[1]

[1]School of Mathematics and Maxwell Institute for Mathematical Sciences, University of Edinburgh, EH9 3FD, UK

[2]Department of Geophysics, Colorado School of Mines, Golden, CO 80401, USA

[3]Scripps Institution of Oceanography, University of California at San Diego, La Jolla, CA 92093-0213, USA

(Received 20 May 2023; revised 21 July 2023; accepted 30 July 2023)

The refraction of surface gravity waves by currents leads to spatial modulations in the wave field and, in particular, in the significant wave height. We examine this phenomenon in the case of waves scattered by a localised current feature, assuming (i) the smallness of the ratio between current velocity and wave group speed, and (ii) a swell-like, highly directional wave spectrum. We apply matched asymptotics to the equation governing the conservation of wave action in the four-dimensional position–wavenumber space. The resulting explicit formulas show that the modulations in wave action and significant wave height past the localised current are controlled by the vorticity of the current integrated along the primary direction of the swell. We assess the asymptotic predictions against numerical simulations using WAVEWATCH III for a Gaussian vortex. We also consider vortex dipoles to demonstrate the possibility of 'vortex cloaking' whereby certain currents have (asymptotically) no impact on the significant wave height. We discuss the role of the ratio of the two small parameters characterising assumptions (i) and (ii) above, and show that caustics are significant only for unrealistically large values of this ratio, corresponding to unrealistically narrow directional spectra.

Key words: surface gravity waves, wave scattering, ocean processes

1. Introduction

Surface gravity waves (SGWs) play a key role in the exchanges of energy, momentum and gases between the ocean and the atmosphere (Villas Bôas & Pizzo 2021). SGWs are forced by the wind and modulated by ocean currents through transport and refraction. Over the

† Email address for correspondence: hannnwangus@gmail.com

© The Author(s), 2023. Published by Cambridge University Press. This is an Open Access article, distributed under the terms of the Creative Commons Attribution licence (http://creativecommons.org/licenses/by/4.0), which permits unrestricted re-use, distribution and reproduction, provided the original article is properly cited.

https://doi.org/10.1017/jfm.2023.686 Published online by Cambridge University Press

past few decades, several studies have explored the effects of ocean currents on SGWs. Early theoretical work focuses on the formation of freak waves and identifies refraction as a possible mechanism for the generation of large-amplitude waves (White & Fornberg 1998; Dysthe, Krogstad & Müller 2008; Heller, Kaplan & Dahlen 2008).

Recent studies examine how mesoscale and submesoscale ocean variability, such as fronts, filaments and vortices, induces a corresponding variability in wave amplitudes (Ardhuin *et al.* 2017; Romero, Lenain & Melville 2017; Romero, Hypolite & McWilliams 2020; Villas Boâs *et al.* 2020; Vrećica, Pizzo & Lenain 2022). These studies often characterise the wave amplitudes using the significant wave height H_s, defined as four times the standard deviation of the surface displacement. They find that wave–current interactions at horizontal scales ranging from 10 to 200 km drive spatial gradients of H_s at similar scales. This indicates that air–sea fluxes might have spatial variability on these relatively small spatial scales.

One common approach to studying wave–current interactions is the use of ray tracing, often in its simplest form in which the kinematics of SGWs is tracked by solving the ray equations, and ray density is used as a proxy for wave amplitude (e.g. Kenyon 1971; Mapp, Welch & Munday 1985; Quilfen & Chapron 2019). While this simple form of ray tracing is a valuable tool for understanding wave refraction, it does not provide an accurate quantification of changes in wave amplitude, in particular changes in H_s. This quantification requires solving the conservation equation for the density of wave action in the four-dimensional position–wavenumber phase space. This is challenging, especially for the wave spectra of realistic sea states, distributed in both wavenumber and direction, instead of the pure plane waves that are often considered (however, see Heller *et al.* 2008). It is possible to solve the action equation numerically, albeit at great computational cost, either by discretising the phase space or by sampling its full four-dimensionality with a large ensemble of rays.

This paper proposes a complementary approach. It develops an asymptotic solution of the wave-action equation, leading to explicit formulas for the changes in action and H_s induced by localised currents. Motivated by their ubiquity in the ocean, we focus on swell, that is, SGWs characterised by a spectrum that is narrow banded in both frequency (equivalently, wavenumber) and direction. We exploit the smallness of two parameters reflecting the narrowness of the spectrum and the weakness of the current relative to the wave speed. We approximate the wave-action equation to leading order, and solve it in closed form by integration along its characteristics (the approximate ray equations) by inspection. The formulas that we obtain show that the changes in action and H_s depend on the currents through a 'deflection function' Δ given by the integral of the vorticity along the primary direction of wave propagation. We apply these formulas to simple flows – vortices and dipoles – and compare their predictions with the results of full integrations of the action conservation equation by a numerical wave model.

We formulate the problem, relate action and H_s, and introduce a model spectrum for swell in § 2. We detail our scaling assumptions and carry out the (matched) asymptotics treatment of the wave-action equation in § 3. We compare asymptotic and numerical results for vortices and dipoles in § 4. For vortices, we consider four different parameter combinations that are representative of ocean swell. We consider dipoles with axis along and perpendicular to the direction of the swell to demonstrate the possibility of a vanishing deflection function Δ, leading to asymptotically negligible changes in H_s, a phenomenon that we refer to as 'vortex cloaking'. In § 5, we explore two limiting regimes of scattering: a linear regime, corresponding to weak currents and/or swell with relatively large angular spread, in which the changes in H_s are linear in the current velocity, and a caustic regime

https://doi.org/10.1017/jfm.2023.686 Published online by Cambridge University Press

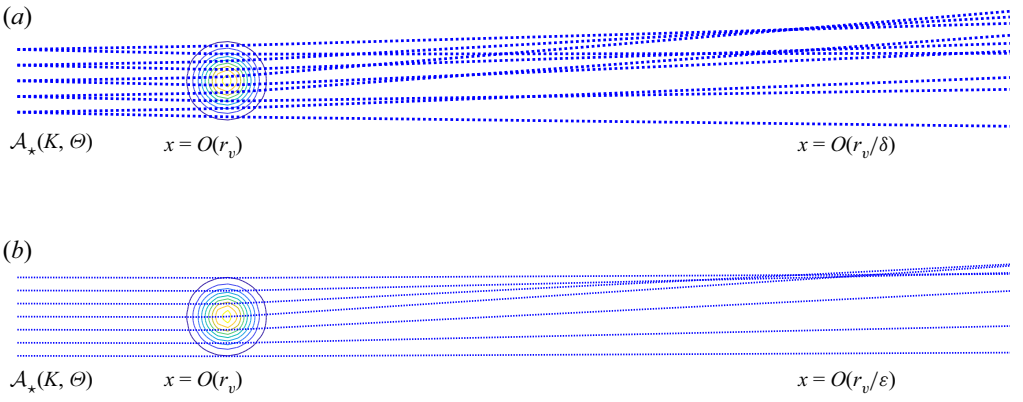


Figure 1. The scattering problem: a localised flow, here shown as an axisymmetric vortex with radius r_v, scatters waves incident from the left ($x \to -\infty$) with action spectrum $\mathcal{A}_\star(K, \Theta)$. Rays bend significantly only in the scattering region in which there is non-zero vorticity, i.e. where $x = O(r_v)$. In this illustration, r_v is equivalent to ℓ_s. (*a*) The case $\delta \neq 0$ ($\gamma = \varepsilon/\delta \ll 1$): directional spreading in the incident spectrum $\mathcal{A}_\star$ is indicated schematically by two rays emanating from each source point. (*b*) The case $\delta = 0$ (or much less than ε; $\gamma = \varepsilon/\delta \gg 1$): the incident spectrum $\mathcal{A}_\star$ is a plane wave with little or no directional spreading.

corresponding to strong currents and/or small angular spread. The caustic regime, in which the changes in H_s are large and concentrated along caustic curves, arises only for parameter values that are outside the range of typical ocean values. We conclude with a summary of our findings and discuss prospects for future work on the spatial variability of H_s in § 6.

2. Formulation

We study the scattering problem sketched in figure 1. Deep-water SGWs, with small initial directional spreading and a well-defined peak frequency (swell), impinge on a spatially compact coherent flow, such as an axisymmetric vortex or a dipole.

2.1. *Action conservation equation*

In figure 1, we illustrate the scattering problem by tracing rays through an axisymmetric vortex. We go beyond ray tracing, however, by using asymptotic methods to obtain approximate analytic solutions of the conservation equation

$$\partial_t \mathcal{A} + \nabla_{\boldsymbol{k}} \omega \cdot \nabla_{\boldsymbol{x}} \mathcal{A} - \nabla_{\boldsymbol{x}} \omega \cdot \nabla_{\boldsymbol{k}} \mathcal{A} = 0 \tag{2.1}$$

for the wave-action density $\mathcal{A}(\boldsymbol{x}, \boldsymbol{k}, t)$ in the four-dimensional position–wavenumber space (Komen *et al.* 1996; Janssen 2004). The action conservation equation (2.1) relies on the WKB assumption of spatial scale separation between waves and currents. In (2.1), $\omega(\boldsymbol{x}, \boldsymbol{k})$ is the absolute frequency of deep-water SGWs:

$$\omega(\boldsymbol{x}, \boldsymbol{k}) = \sigma(k) + \boldsymbol{k} \cdot \boldsymbol{U}(\boldsymbol{x}). \tag{2.2}$$

We consider deep-water waves so that in (2.2) the intrinsic frequency is $\sigma(k) = \sqrt{gk}$, with $k = |\boldsymbol{k}|$. The current velocity is taken to be horizontal and independent of time and depth:

$$\boldsymbol{U}(\boldsymbol{x}) = U(x, y)\,\hat{\boldsymbol{x}} + V(x, y)\,\hat{\boldsymbol{y}}. \tag{2.3}$$

The wave-action equation (2.1) provides a phase-averaged description of the scattering problem made possible by the scale separation between waves and currents. This places

https://doi.org/10.1017/jfm.2023.686 Published online by Cambridge University Press

our work in contrast to that of Coste, Lund & Umeki (1999), Coste & Lund (1999) and McIntyre (2019), who examined scattering without the simplification afforded by scale separation, and discuss phase effects such as the Aharonov–Bohm effect. We also assume fixed currents and do not consider how these might be modified by the presence of waves (see e.g. Humbert, Aumaître & Gallet 2017; McIntyre 2019).

2.2. *Action spectrum and significant wave height*

Denoting the sea-surface vertical displacement by $\zeta(\boldsymbol{x}, t)$, with root-mean-square ζ_{rms}, and following Komen *et al.* (1996), we introduce a spectrum $\mathcal{F}(\boldsymbol{k}, \boldsymbol{x}, t)$ such that

$$\zeta_{rms}^2(\boldsymbol{x}, t) = \int \mathcal{F}(\boldsymbol{k}, \boldsymbol{x}, t)\, \mathrm{d}\boldsymbol{k}. \tag{2.4}$$

Later, we use a polar coordinate system (k, θ) in $\boldsymbol{k}$ space so that in (2.4), $\mathrm{d}\boldsymbol{k} = k\, \mathrm{d}k\, \mathrm{d}\theta$. The kinetic and potential energy densities for deep-water SGWs are equipartitioned so that the energy spectrum is $g\mathcal{F}$ and the action spectrum – $\mathcal{A}(\boldsymbol{x}, \boldsymbol{k}, t)$ in (2.1) – is $\mathcal{A} = g\mathcal{F}/\sigma$. The significant wave height $4\zeta_{rms}$ (Komen *et al.* 1996) is therefore

$$H_s(\boldsymbol{x}, t) = \left(\frac{16}{g} \int \mathcal{A}(\boldsymbol{k}, \boldsymbol{x}, t)\, \sigma(k)\, \mathrm{d}\boldsymbol{k} \right)^{1/2}. \tag{2.5}$$

The incident swell is characterised by a spatially uniform spectrum $\mathcal{F}_\star(\boldsymbol{k})$ with constant significant wave height $H_{s\star}$. The subscript $\star$ denotes quantities associated with the incident waves. Swell is characterised by a narrow spectrum in both wavenumber k (equivalently, frequency σ) and direction θ. The dominant wavenumber of the incident swell is $k_\star$ with frequency $\sigma_\star = \sqrt{gk_\star}$, and the dominant direction is taken without loss of generality as $\theta = 0$. Thus, as illustrated in figure 1, the waves arrive from $x = -\infty$ and impinge on an isolated flow feature, centred at $(x, y) = (0, 0)$. As an example of incident spectrum, we use a separable construction described in Appendix A. In the narrow-band limit corresponding to swell, this spectrum simplifies to the Gaussian

$$\mathcal{F}_\star(k, \theta) \approx \zeta_{rms\star}^2 \underbrace{\frac{\exp(-(k-k_\star)^2/2\delta_k^2)}{k_\star\sqrt{2\pi\delta_k^2}}}_{F_\star(k)} \times \underbrace{\frac{\exp(-\theta^2/2\delta_\theta^2)}{\sqrt{2\pi\delta_\theta^2}}}_{D_\star(\theta)}. \tag{2.6}$$

The two parameters δ_k and δ_θ capture the wavenumber and directional spreading (see Appendix A). The narrow-band limit assumes that $\delta_k/k_\star \ll 1$ and $\delta_\theta \ll 1$.

3. The scattering problem

We consider an incident spectrum such as (2.6). To make its localisation in k and θ explicit, we introduce the $O(1)$ independent variables

$$K = \frac{k - k_\star}{\delta} \quad \text{and} \quad \Theta = \frac{\theta}{\delta}, \tag{3.1a,b}$$

where $\delta \ll 1$ is a small dimensionless parameter. The incident action spectrum has the form

$$\mathcal{A}(x, y, k, \theta) = \mathcal{A}_\star(K, \Theta) \quad \text{as } x \to -\infty, \tag{3.2}$$

with the function $\mathcal{A}_\star(K, \Theta)$ localised where both K and Θ are $O(1)$. The example spectrum (2.6) is of this form provided that $\delta_k/k_\star$ and δ_θ are both $O(\delta)$. This assumption

https://doi.org/10.1017/jfm.2023.686 Published online by Cambridge University Press

of similarly small spectral widths in k and θ enforces the relevant distinguished limit for the scattering problem.

We assume that the currents are weak (e.g. Peregrine 1976; Villas Bôas & Young 2020). This means that the typical speed U of the currents is much less than the intrinsic group velocity of the incident swell $c_\star$:

$$\varepsilon \overset{\text{def}}{=} U/c_\star, \tag{3.3}$$

$$\ll 1. \tag{3.4}$$

Accordingly, we rewrite the frequency (2.2) as

$$\omega(\boldsymbol{x}, \boldsymbol{k}) = \sigma(k) + \varepsilon \boldsymbol{k} \cdot \boldsymbol{U}(\boldsymbol{x}). \tag{3.5}$$

We indulge in a slight abuse of notation here: we develop the approximation in dimensional variables, hence the dimensionless parameters ε and δ in expressions such as (3.1*a*,*b*) and (3.5) should be interpreted as bookkeeping parameters to be set to 1 at the end. We examine the distinguished limit

$$\delta, \varepsilon \to 0 \quad \text{with } \gamma \overset{\text{def}}{=} \varepsilon/\delta = O(1), \tag{3.6}$$

and use matched asymptotics to solve the action conservation equation (2.1). We emphasise that $\gamma = O(1)$ is a formal assumption that enables us to capture the broadest range of relative size of ε and δ, including $\varepsilon \ll \delta$ and $\delta \ll \varepsilon$ (see § 5).

3.1. *The scattering region: $x = O(\ell_s)$*

The spatially compact flow has a typical horizontal length scale that we denote by ℓ_s. We refer to the region where $x = O(\ell_s)$ as the 'scattering region'. The solution in this region has the form

$$\mathcal{A}(K, \Theta, x, y), \tag{3.7}$$

and must limit to $\mathcal{A}_\star(K, \Theta)$ in (3.2) as $x \to -\infty$.

With $\mathcal{A}$ in (3.7), the transport term in (2.1) is approximated as

$$\begin{aligned} \boldsymbol{\nabla}_{\boldsymbol{k}}\omega \cdot \boldsymbol{\nabla}_{\boldsymbol{x}}\mathcal{A} &= c_\star \left(\cos(\delta\Theta)\, \mathcal{A}_x + \sin(\delta\Theta)\, \mathcal{A}_y\right) + \varepsilon \boldsymbol{U} \cdot \boldsymbol{\nabla}_{\boldsymbol{x}}\mathcal{A} \\ &= c_\star \mathcal{A}_x + O(\delta, \varepsilon). \end{aligned} \tag{3.8}$$

In particular, transport by the current $\varepsilon \boldsymbol{U} \cdot \boldsymbol{\nabla}_{\boldsymbol{x}}\mathcal{A}$ is negligible compared with transport by the intrinsic group velocity $c_\star$. With the approximations

$$\boldsymbol{\nabla}_{\boldsymbol{k}}\mathcal{A} = \delta^{-1}\left(\partial_K \mathcal{A}\, \hat{\boldsymbol{x}} + k_*^{-1}\, \partial_\Theta \mathcal{A}\, \hat{\boldsymbol{y}}\right) + O(1), \tag{3.9}$$

$$\boldsymbol{\nabla}_{\boldsymbol{x}}\omega = \varepsilon k_\star (U_x \hat{\boldsymbol{x}} + U_y \hat{\boldsymbol{y}}) + O(\varepsilon\delta), \tag{3.10}$$

the refraction term in (2.1) simplifies to

$$\boldsymbol{\nabla}_{\boldsymbol{x}}\omega \cdot \boldsymbol{\nabla}_{\boldsymbol{k}}\mathcal{A} = \gamma \left(k_\star U_x\, \partial_K \mathcal{A} + U_y\, \partial_\Theta \mathcal{A}\right) + O(\varepsilon). \tag{3.11}$$

Thus in the scattering region, the leading-order approximation to (2.1) is

$$c_\star\, \partial_x \mathcal{A} - \gamma \left(k_\star U_x\, \partial_K \mathcal{A} + U_y\, \partial_\Theta \mathcal{A}\right) = 0. \tag{3.12}$$

One might solve (3.12) using its characteristics – the ray equations – or by inspection. By either method, the solution to (3.12) that matches the incident action spectrum (3.2) as

https://doi.org/10.1017/jfm.2023.686 Published online by Cambridge University Press

$x \to -\infty$ is found to be

$$\mathcal{A}(x, y, K, \Theta) = \mathcal{A}_\star \left(K + \frac{\gamma k_\star}{c_\star} U(x, y), \Theta + \frac{\gamma}{c_\star} \int_{-\infty}^{x} U_y(x', y)\, \mathrm{d}x' \right). \tag{3.13}$$

It is insightful to introduce the vorticity $Z \overset{\text{def}}{=} V_x - U_y$ and write (3.13) as

$$\mathcal{A}(x, y, K, \Theta) = \mathcal{A}_\star \left(K + \frac{\gamma k_\star}{c_\star} U(x, y), \Theta + \frac{\gamma}{c_\star} V(x, y) - \frac{\gamma}{c_\star} \int_{-\infty}^{x} Z(x', y)\, \mathrm{d}x' \right). \tag{3.14}$$

For reference, we rewrite this expression in terms of the original independent variables, setting the bookkeeping parameters ε, δ and hence γ to 1 to obtain

$$\mathcal{A}(x, y, k, \theta) = \mathcal{A}_\star \left(k + \frac{k_\star}{c_\star} U(x, y), \theta + \frac{1}{c_\star} V(x, y) - \frac{1}{c_\star} \int_{-\infty}^{x} Z(x', y)\, \mathrm{d}x' \right). \tag{3.15}$$

3.2. *The intermediate region: $O(\ell_s) \ll x \ll O(\ell_s/\delta)$*

The outer limit of the inner solution (3.14) follows from taking $x \to \infty$:

$$\mathcal{A}(x, y, K, \Theta) \to \mathcal{A}_\star \left(K, \Theta - \gamma\, \Delta(y) \right), \tag{3.16}$$

where we have introduced the dimensionless 'deflection'

$$\Delta(y) \overset{\text{def}}{=} \frac{1}{c_\star} \int_{-\infty}^{\infty} Z(x', y)\, \mathrm{d}x'. \tag{3.17}$$

According to (3.16), the effect of the flow on the dependence of $\mathcal{A}$ on K is reversible: after passage through the scattering region, this dependence reverts to the incident form. In contrast, there is a net change in Θ, quantified by the deflection $\Delta(y)$. This can be related to classical scattering of particles by viewing y as the impact parameter of a wavepacket. The scattering cross-section, defined as $\mathrm{d}y/\mathrm{d}\theta_\infty$, where θ_∞ is the angle of propagation of the wavepacket as $x \to \infty$, is then $-1/(\varepsilon\, \Delta'(y))$.

To interpret (3.16) and $\Delta(y)$ physically, recall that if ε is small, then

$$\text{ray curvature} \approx \frac{\text{vorticity}}{\text{group velocity}}, \tag{3.18}$$

$$\approx \frac{Z(x, y)}{c_\star}. \tag{3.19}$$

The approximation in (3.18) requires only $\varepsilon \ll 1$ (e.g. Kenyon 1971; Dysthe 2001; Landau & Lifshitz 2013; Gallet & Young 2014). Passing from (3.18) to (3.19) requires the further approximation that k is close to $k_\star$ so that the group velocity in the denominator of (3.18) can be approximated by the constant $c_\star$. On the left-hand side of (3.18), ray curvature is $\mathrm{d}\theta/\mathrm{d}\ell$, where ℓ is arc length along a ray. But within the compact scattering region, we approximate ℓ with x. Thus the deflection $\Delta(y)$ in (3.17) is the integrated ray curvature, accumulated as rays pass through the scattering region in which $x = O(\ell_s)$ and vorticity $Z(x, y)$ is non-zero.

From (3.17) and (3.18), we conclude that the scattering region is best characterised as the region with $O(1)$ vorticity, e.g. the vortex core in figure 1 (hence $\ell_s = r_v$, with r_v a typical vortex radius). The region with palpably non-zero velocity is much larger. In figure 1, the rays are straight where $x = O(r_v/\varepsilon)$, despite the slow ($\propto r^{-1}$) decay of the azimuthal vortex velocity.

https://doi.org/10.1017/jfm.2023.686 Published online by Cambridge University Press

3.3. *The far field: $x = O(\ell_s/\delta)$*

Far from the scattering region, where $x \gg \ell_s$, we introduce the slow coordinate $X \overset{\text{def}}{=} \delta x$. In the far field, the currents and hence the refraction term $\boldsymbol{\nabla}_{\boldsymbol{x}}\omega \cdot \boldsymbol{\nabla}_{\boldsymbol{k}}\mathcal{A}$ in (2.1) are negligible. The steady action conservation equation collapses to

$$\boldsymbol{\nabla}_{\boldsymbol{k}}\sigma \cdot \boldsymbol{\nabla}_{\boldsymbol{x}}\mathcal{A} = c_\star \left(\delta \cos(\delta\Theta)\, \mathcal{A}_X + \sin(\delta\Theta)\, \mathcal{A}_y\right) = 0, \tag{3.20}$$

i.e. propagation along straight rays. Retaining only the leading-order term gives

$$\partial_X \mathcal{A} + \Theta\, \partial_y \mathcal{A} = 0. \tag{3.21}$$

By inspection, the solution of (3.21) that matches the intermediate solution (3.16) is

$$\mathcal{A}(X, y, K, \Theta) = \mathcal{A}_\star\left(K, \Theta - \gamma\, \Delta\,(y - X\Theta)\right). \tag{3.22}$$

This formula, which converts the incident spectrum into the far-field spectrum, is a key result of the paper. In terms of the original independent variables and with the bookkeeping parameters set to 1, it takes the convenient form

$$\mathcal{A}(x, y, k, \theta) = \mathcal{A}_\star\left(k, \theta - \Delta\,(y - x\theta)\right). \tag{3.23}$$

3.4. *Significant wave height*

Significant wave height H_s is the most commonly reported statistic of wave amplitudes, being observed routinely by satellite altimeters and wave buoys. We obtain an approximation for H_s by performing the k and θ integrals in (2.5) using the approximations (3.15) and (3.23) for $\mathcal{A}(\boldsymbol{x}, \boldsymbol{k})$.

The scattering region is simple. We can approximate σ and $\mathrm{d}\boldsymbol{k}$ in (2.5) by $\sigma_\star = \sigma(k_\star)$ and $k_\star\, \mathrm{d}k\, \mathrm{d}\theta$ to find

$$H_s(\boldsymbol{x}, t) \sim \left(\frac{16\sigma_\star k_\star}{g} \iint \mathcal{A}(\boldsymbol{k}, \boldsymbol{x}, t)\, \mathrm{d}k\, \mathrm{d}\theta\right)^{1/2} \tag{3.24}$$

$$\sim H_{s\star}. \tag{3.25}$$

The second equality holds because, according to (3.15), $\mathcal{A}(\boldsymbol{x}, \boldsymbol{k})$ is obtained from $\mathcal{A}_\star(\boldsymbol{x}, \boldsymbol{k})$ by an $\boldsymbol{x}$-dependent shift of k and θ that does not affect the integral. Thus H_s in the scattering region is unchanged from the incident value $H_{s\star}$. This conclusion also follows directly from steady-state wave-action conservation under the assumptions $\varepsilon, \delta \ll 1$: multiplying (3.12) by $\sigma_\star k_\star$ and integrating over k and θ, we find

$$c_\star\, \partial_x \underbrace{\left(\sigma_\star k_\star \iint \mathcal{A}(\boldsymbol{x}, \boldsymbol{k})\, \mathrm{d}k\, \mathrm{d}\theta\right)}_{\approx g\, H_s^2(\boldsymbol{x})/16} = 0. \tag{3.26}$$

Hence $H_s(\boldsymbol{x}) = H_{s\star}$ throughout the scattering region.

https://doi.org/10.1017/jfm.2023.686 Published online by Cambridge University Press

In the far field, H_s is obtained by substituting (3.23) into (2.5). The result is

$$H_s(\boldsymbol{x}) = 4\sqrt{\frac{k_\star\sigma_\star}{g}\int \mathrm{d}\theta \int \mathrm{d}k\, \mathcal{A}_\star(k, \theta - \Delta(y - x\theta))}. \tag{3.27}$$

The k integral can be evaluated in terms of the incident directional spectrum, which, in the general case of a non-separable spectrum, is defined as

$$D_\star(\theta) \overset{\text{def}}{=} \frac{1}{\zeta_{rms\star}^2}\int \mathcal{F}_\star(\boldsymbol{k})\, k\, \mathrm{d}k. \tag{3.28}$$

We summarize the results above with

$$H_s(\boldsymbol{x}) = H_{s\star}\begin{cases} 1 & \text{in the scattering region,} \\ \sqrt{\int D_\star\,(\theta - \Delta(y - x\theta))\,\mathrm{d}\theta} & \text{in the far field.} \end{cases} \tag{3.29}$$

4. Applications to simple flows

4.1. *Gaussian vortex*

As an application, we consider scattering by an axisymmetric Gaussian vortex with circulation κ, vorticity

$$Z(x, y) = \frac{\kappa \exp(-r^2/2r_v^2)}{2\pi r_v^2}, \tag{4.1}$$

and velocity

$$(U(x, y), V(x, y)) = \frac{\kappa}{2\pi}\,\frac{1 - \exp(-r^2/2r_v^2)}{r^2}\,(-y, x), \tag{4.2}$$

where $r^2 = x^2 + y^2$. The vortex radius r_v can be taken as the scattering length scale ℓ_s. The maximum azimuthal velocity is $U_m = 0.072\,\kappa/r_v$ at radius $1.585\,r_v$. The deflection (3.17) resulting from this Gaussian vortex is

$$\Delta(y) = \frac{\kappa \exp(-y^2/2r_v^2)}{\sqrt{2\pi}\, r_v c_\star}. \tag{4.3}$$

The asymptotic solution in the scattering region is obtained from (3.15) as

$$\mathcal{A}(x, y, k, \theta) = \mathcal{A}_\star\big(k + k_* c_*^{-1}\, U(x, y), \theta + c_*^{-1}\, V(x, y) - \tfrac{1}{2}\big(\mathrm{erf}(x/\sqrt{2}r_v) + 1\big)\Delta(y)\big), \tag{4.4}$$

where erf is the error function. Equation (4.4) can be combined with the far-field approximation (3.23) into a single, uniformly valid approximation:

$$\begin{aligned}&\mathcal{A}(x, y, k, \theta)\\ &\quad = \mathcal{A}_\star\big(k + k_* c_*^{-1}\, U(x, y), \theta + c_*^{-1}\, V(x, y) - \tfrac{1}{2}\big(\mathrm{erf}(x/\sqrt{2}r_v) + 1\big)\Delta(y - x\theta)\big).\end{aligned} \tag{4.5}$$

The significant wave height is approximated by (3.29), which can be written as the uniform expression

$$H_s(x, y) = H_{s\star}\sqrt{\int D_\star\left(\theta - \Delta(y - x^+\theta)\right)\mathrm{d}\theta}, \tag{4.6}$$

where x^+ is equal to x for $x > 0$ and to 0 for $x < 0$, and (4.3) is used for Δ.

https://doi.org/10.1017/jfm.2023.686 Published online by Cambridge University Press

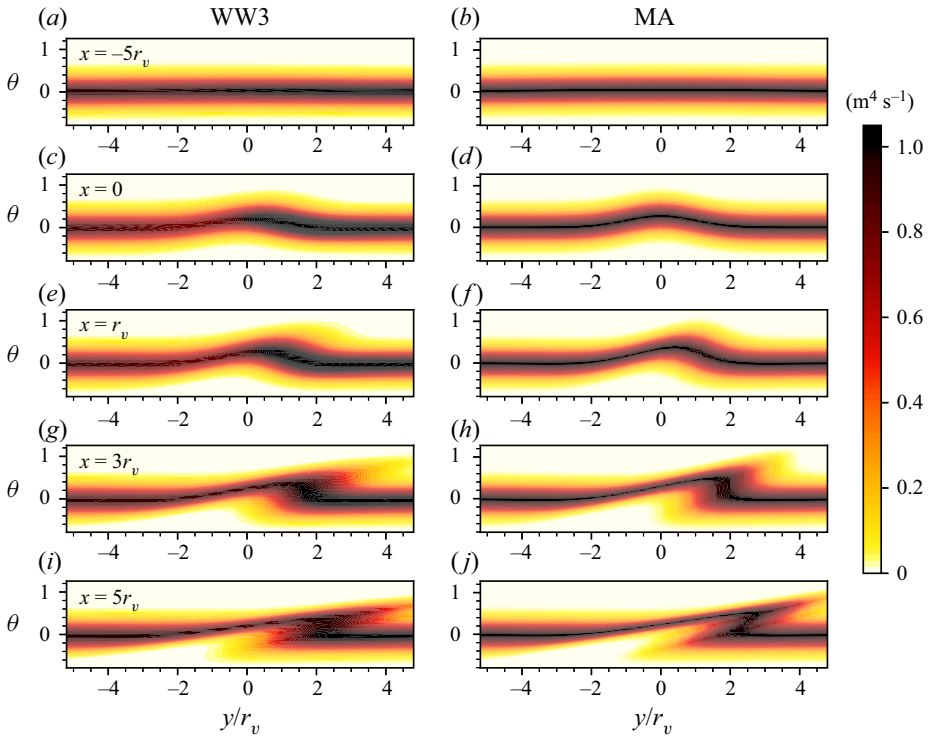


Figure 2. Wavenumber-integrated action density $\int \mathcal{A}(x, y, k, \theta)\,\mathrm{d}k$ as a function of y and θ at x-values (*a*,*b*) $-5r_v$, (*c*,*d*) 0, (*e*,*f*) r_v, (*g*,*h*) $3r_v$, and (*i*,*j*) $5r_v$, from (*a*,*c*,*e*,*g*,*i*) WW3 and (*b*,*d*,*f*,*h*,*j*) MA (see (4.5)), for swell impinging on a Gaussian vortex with $U_m = 0.8$ m s^{-1}. The directional spreading of the incident spectrum is $s = 40$.

We now compare the matched asymptotic (MA) predictions (4.5)–(4.6) with numerical solutions of the wave-action equation (2.1) obtained with the wave height, water depth, and current hindcasting third-generation wave model (WAVEWATCH III, hereafter WW3). The incident spectrum used for WW3 is described in Appendix A. The directional function for this spectrum is the Longuet-Higgins, Cartwright & Smith (1963) model

$$D_\star(\theta) \propto \cos^{2s}\frac{\theta}{2}. \tag{4.7}$$

The parameter $s > 0$ controls the directional spreading: for $s \gg 1$, (4.7) reduces to the Gaussian in (2.6) with directional spreading $\delta_\theta = \sqrt{2/s}$. The configuration of WW3 and spectrum parameters are detailed in Appendix B. The most important parameter is the peak frequency of the incident spectrum, taken fixed for all simulations as $\sigma_\star = 0.61$ rad s^{-1}. This corresponds to the period 10.3 s, wavelength 166 m and group speed $c_\star = 8$ m s^{-1}. Because the problem is linear in the action density, the values of $\zeta_{rms\star}$, or equivalently $H_{s\star}$, are less important. For definiteness, we set $H_{s\star} = 1$ m.

Figure 2 compares the wavenumber-integrated wave action $\int \mathcal{A}(x, y, k, \theta)\,\mathrm{d}k$ obtained from (4.5) and WW3 for a Gaussian vortex with maximum velocity $U_m = 0.8$ m s^{-1} and directional spreading parameter $s = 40$, showing good agreement, especially in the far-field region ($x \geqslant 3r_v$). The most noticeable difference between MA and WW3 is in figures 2(*c*,*d*), which show a section through the middle of the vortex. The MA action

https://doi.org/10.1017/jfm.2023.686 Published online by Cambridge University Press

s	U_m (m s^{-1})	$\delta = \sqrt{2/s}$	$\varepsilon = U_m/c_\star$	$\gamma = \varepsilon/\delta$
10	0.4	0.447 (25.6°)	0.05	0.112
40	0.4	0.224 (12.8°)	0.05	0.224
10	0.8	0.447 (25.6°)	0.1	0.224
40	0.8	0.224 (12.8°)	0.1	0.447

Table 1. Parameters corresponding to each configuration in § 4.1, arranged in the order of the rows in figure 3. In all cases, the group speed is $c_\star = 8$ m s^{-1}, corresponding to wavelength 166 m and period 10.3 s. Here, U_m is the maximum vortex velocity, and the vortex radius is $r_v = 25$ km.

spectrum in figure 2(d) is obtained via a y-dependent shift in $\mathcal{A}_\star(k, \theta)$; there is no change in the intensity of $\mathcal{A}$ associated with this shift. In figure 2(c), on the other hand, the intensity of the WW3 action spectrum varies with y/r_v. We attribute this difference to asymptotically small effects such as the contribution $\boldsymbol{U} \cdot \nabla_{\boldsymbol{x}} \mathcal{A}$ to wave-action transport.

In the remainder of this section, we assess the dependence of significant wave height H_s on the directional spreading parameter s and flow strength U_m. We consider the four different combinations of s and U_m given in table 1. The corresponding values of the dimensionless parameters, taken as

$$\delta = \delta_\theta = \sqrt{2/s} \quad \text{and} \quad \varepsilon = U_m/c_\star, \tag{4.8a,b}$$

are also in the table.

Typically, observations of the directional spreading for swell are in the range 10°–20° (Ewans 2002), which corresponds to a range for s between 16 and 66. In our experiments, setting $s = 10$ and $s = 40$ leads to directional spreading of 24° and 12°, respectively, which correspond to very broad and very narrow swells.

Figures 3 and 4 show the significant wave height anomaly

$$h_s(\boldsymbol{x}) \overset{\text{def}}{=} H_s(\boldsymbol{x}) - H_{s\star} \tag{4.9}$$

for each combination of s and U_m. Because of our choice $H_{s\star} = 1$ m, h_s in cm can be interpreted as the fractional change in significant wave height expressed as a percentage. A control run of WW3 in the absence of currents shows that h_s is not exactly zero but decreases slowly with x. This is caused by the finite y-extent of the computational domain that leads to a wave forcing with compact support. To mitigate this numerical artefact, we compute the WW3 significant wave height anomaly as $h_s(\boldsymbol{x}) = H_s(\boldsymbol{x}) - H_s^{ctrl}(\boldsymbol{x})$, where $H_s^{ctrl}(\boldsymbol{x})$ is the significant wave height of the current-free control run. See Appendix B for details.

Figures 3 and 4 show that h_s has a wedge-like pattern in the wake of the vortex resulting from wave focusing and defocusing, with $h_s > 0$ mainly for $y > 0$, and $h_s < 0$ for $y < 0$. The pattern is not antisymmetric about $y = 0$, and positive anomalies are larger than negative anomalies. These characteristics, which indicate a nonlinear response, are increasingly marked as s and U_m increase. Specifically, the parameter

$$\gamma = \frac{\varepsilon}{\delta} = \frac{U_m}{c_\star}\sqrt{\frac{s}{2}} \tag{4.10}$$

controls the degree of nonlinearity and hence of asymmetry. We discuss the two limiting regimes $\gamma \ll 1$ and $\gamma \gg 1$ in § 5.

https://doi.org/10.1017/jfm.2023.686 Published online by Cambridge University Press

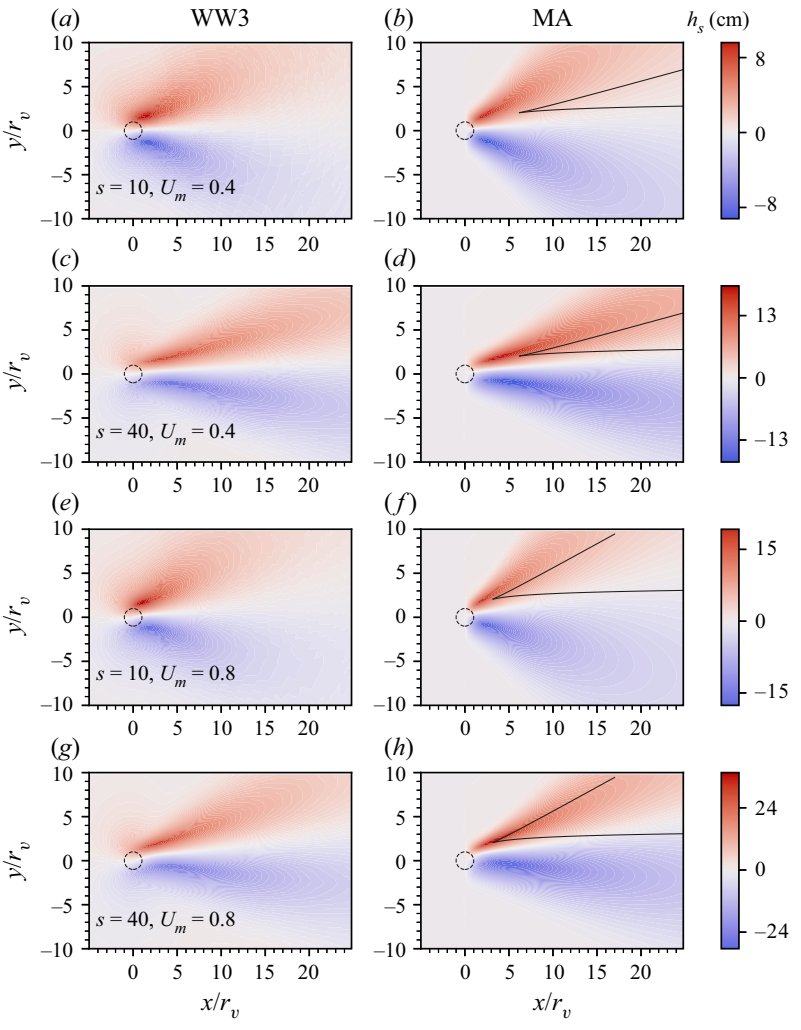


Figure 3. Significant wave height anomaly $h_s(x, y)$ from (a,c,e,g) WW3 and (b,d,f,h) MA, for swell impinging on a Gaussian vortex. Each row corresponds to the indicated values of the directional spreading parameter s of the incident wave spectrum, and the maximum velocity U_m (in m s^{-1}). The corresponding non-dimensional parameters are given in table 1. The dashed circles have radius r_v around the vortex centre. The solid lines in (b,d,f,h) indicate the caustics computed from (D6). The colour bars differ between rows but are the same within each row. White corresponds to $h_s = 0$ in all plots. The customizable notebook that generates (h) by default can be accessed at https://www.cambridge.org/S0022112023006869/JFM-Notebooks/files/Figure-3.ipynb.

There is good overall agreement between WW3 and MA, even though in the case $s = 10$, the parameter $\delta = 0.447$ is only marginally small. The pattern is more diffuse for WW3 than for MA, with a less sharply defined wedge and a non-zero h_s over a larger proportion of the domain. We attribute the differences to the finiteness of δ (they are more marked for $s = 10$, $\delta = 0.447$ than for $s = 40$, $\delta = 0.224$), and to the limited spectral resolution of WW3 (simulations with degraded angular resolution lead to an even more diffuse h_s). The most conspicuous differences between WW3 and MA appear in the scattering region, where the non-zero h_s obtained with WW3 appears to contradict the MA prediction that $h_s = 0$. The non-zero h_s results from $O(\varepsilon, \delta)$ terms neglected by MA. Relaxing some of

https://doi.org/10.1017/jfm.2023.686 Published online by Cambridge University Press

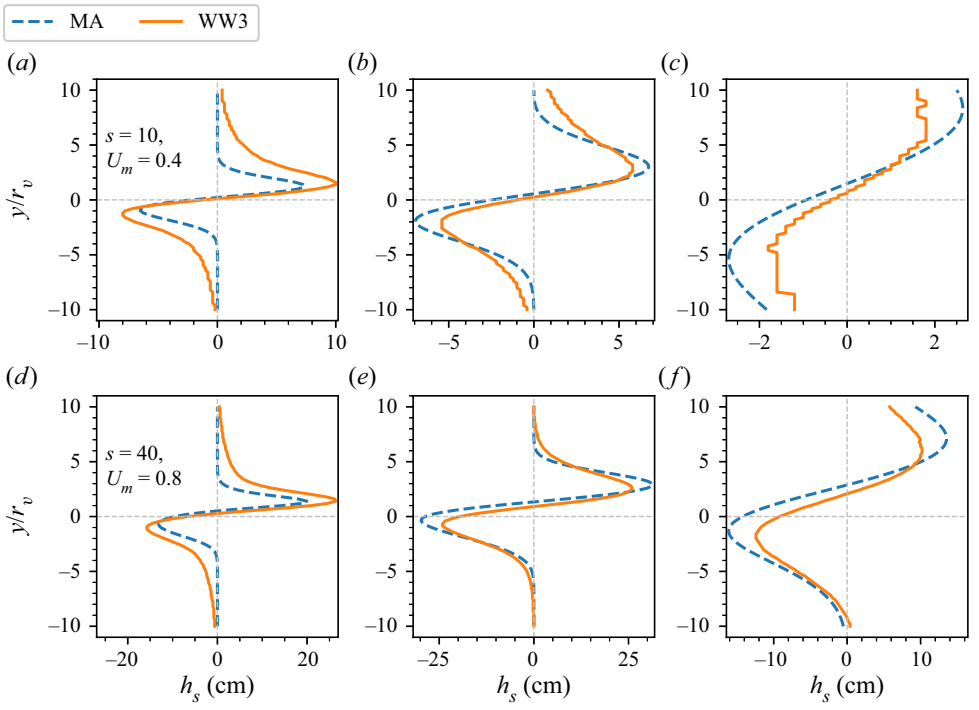


Figure 4. Significant wave height anomaly h_s as a function of y for (*a*,*d*) $x = r_v$, (*b*,*e*) $x = 5r_v$, (*c*,*f*) $x = 15r_v$, and from WW3 (solid lines) and MA (see (4.5), dashed lines) in the set-up of figure 3. Results are shown for two sets of parameters s and U_m as indicated in (*a*,*d*). The range of h_s differs between plots.

the approximations leading to (3.24) gives a heuristic correction to MA that captures the bulk of the difference with WW3 in the scattering region. We explain this in Appendix C.

As further demonstration of the MA approach, we provide a Jupyter notebook accessible at https://www.cambridge.org/S0022112023006869/JFM-Notebooks/files/Figure-3.ipynb, where users can customize the form of the current and the incoming wave spectrum to experiment with the resulting $\int \mathcal{A}(x, y, k, \theta)\, \mathrm{d}k$ and h_s.

4.2. *Vortex dipole*

A striking feature of the far-field spectrum and hence of H_s is that, according to MA, they depend on the flow only through the deflection $\Delta(y)$ in (3.17), proportional to the integral of the vorticity along the direction of dominant wave propagation (the x-direction in our set-up). This implies that if the integrated vorticity vanishes because of cancellations between positive and negative contributions, the differences between far-field and incident fields are asymptotically small. This can be interpreted as a form of 'vortex cloaking', whereby an observer positioned well downstream of a flow feature is unable to detect its presence through changes in wave statistics. We demonstrate this phenomenon by examining the scattering of swell by vortex dipoles.

We consider two cases, corresponding to dipoles whose axes (the vectors joining the centres of positive and negative vorticity) are, respectively, perpendicular and parallel to the direction of wave propagation. The corresponding vorticity fields are chosen, up to a constant multiple, as the derivative of the Gaussian profile (4.1) with respect to y or x.

https://doi.org/10.1017/jfm.2023.686 Published online by Cambridge University Press

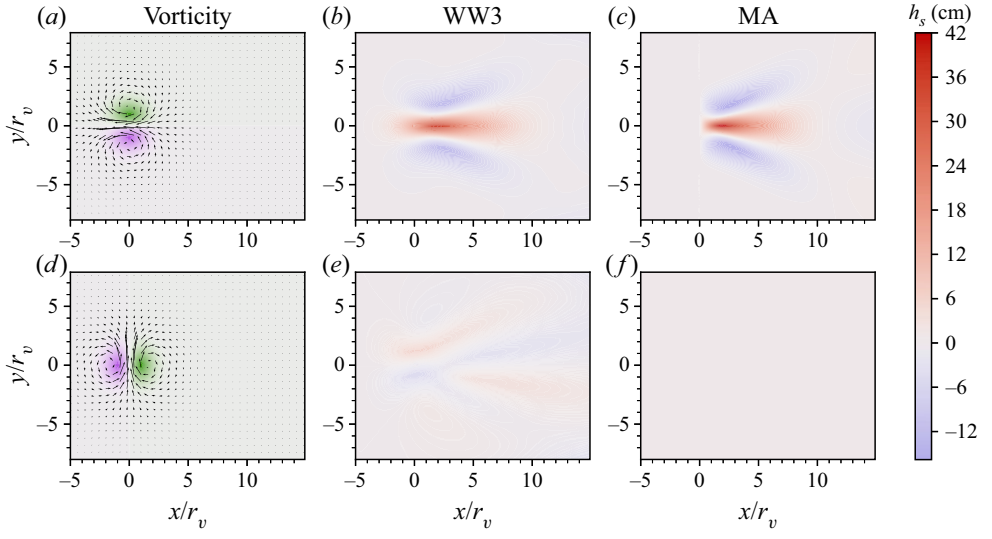


Figure 5. Swell impinging on vortex dipoles with axes (*a–c*) perpendicular and (*d–f*) parallel to the dominant direction of wave propagation (*x*-axis). The vorticity (colour) and velocity (vectors) are shown in (*a*,*d*), together with the significant wave height anomaly h_s from WW3 in (*b*,*e*) and MA in (*c*,*f*). The directional spreading parameter is $s = 40$, and the maximum flow velocity is 0.8 m s^{-1}.

Figure 5 shows the significant wave height anomaly obtained for the incident spectrum of § 4.1 with $s = 40$ and dipoles with maximum velocity $U_m = 0.8\text{m s}^{-1}$.

When the dipole axis is in the y-direction (figures 5*a–c*), the deflection $\Delta(y)$ does not vanish identically. As a result, H_s is affected strongly by the flow, for our choice of parameters. This applies to both the MA and WW3 predictions, which match closely in the far field. When the dipole axis is in the x-direction (figures 5*d–f*), $\Delta(y) = 0$. The MA prediction is then that $H_s = H_{s\star}$, i.e. $h_s = 0$ everywhere. The WW3 simulation is consistent with this, with only a weak signal in h_s.

In general, for a dipole with axis making an angle α with the direction of wave propagation, the deflection $\Delta(y)$ is proportional to $\sin\alpha$, and the cloaking effect is partial unless $\alpha = 0$.

5. Limiting cases

In this section, we return to the far-field asymptotics (3.22) for $\mathcal{A}$ in terms of the scaled dependent variables in order to examine two limiting regimes characterised by extreme values of $\gamma = \varepsilon/\delta$. The regime $\gamma \ll 1$ corresponds to a weak flow and/or relatively broad spectrum, leading to a linear dependence of h_s on the currents. The opposite regime $\gamma \gg 1$ corresponds to strong flow and/or a highly directional spectrum. The wave response is then highly nonlinear in the currents and, as we show below, controlled by the caustics that exist for pure plane incident waves ($\gamma = \infty$). The 'freak index' of Heller *et al.* (2008), given by $\varepsilon^{2/3}/\delta$, is the analogue of γ for spatially extended, random currents.

5.1. *Linear regime:* $\gamma \ll 1$

For $\gamma \ll 1$, we can expand (3.22) in Taylor series to obtain

$$\mathcal{A}(X, y, K, \Theta) = \mathcal{A}_\star(K, \Theta) - \gamma\, \Delta(y - X\Theta)\, \partial_\Theta \mathcal{A}_\star(K, \Theta) + O(\gamma^2). \tag{5.1}$$

https://doi.org/10.1017/jfm.2023.686 Published online by Cambridge University Press

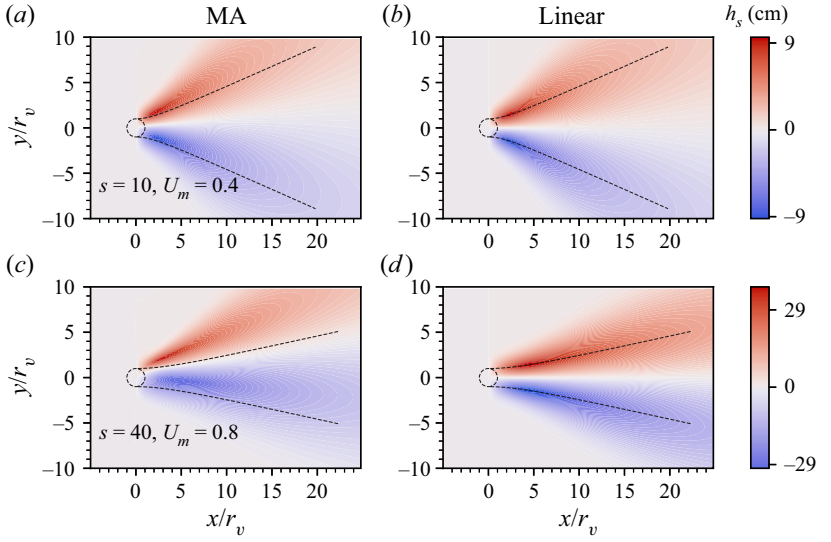


Figure 6. Significant wave height anomaly $h_s(x, y)$ for swell impinging on a Gaussian vortex: comparison between the predictions of (a,c) MA and (b,d) its $\gamma \to 0$ limit (see (5.3)). The set-up is as in figure 3, with parameters s and U_m (in m s^{-1}) as indicated. Dashed lines indicates the curves $y = \pm\sqrt{r_v^2 + 2x^2/s}$ where h_s reaches maximum amplitudes according to (5.3).

This indicates that the flow induces the small correction $-\gamma\, \Delta(y - X\Theta)\, \partial_\Theta \mathcal{A}_\star(K, \Theta)$ to the action of the incident wave. We deduce an approximation for H_s by integrating (5.1) with respect to K and Θ to obtain H_s^2 followed by a Taylor expansion of a square root. Alternatively, we can carry out a Taylor expansion of the far-field approximation (3.29) of H_s, treating $\Delta(y)$ as small. The result is best expressed in terms of the anomaly h_s, found to be

$$h_s(x, y) = -\frac{H_{s\star}}{2} \int D_s'(\theta)\, \Delta(y - x\theta)\, \mathrm{d}\theta \tag{5.2}$$

after reverting to the unscaled variables and setting $\gamma = 1$. This simple expression is evaluated readily once the flow, hence $\Delta(y)$, and directional spectrum $D_\star(\theta)$ are specified. For the Gaussian vortex of § 4.1 and the directional spectrum in (2.6), the integration can be carried out explicitly, yielding

$$h_s(x, y) = \frac{H_{s\star}\kappa}{c_\star\sqrt{\pi}}\, \frac{x^+ y \exp\!\big(-y^2/(2r_v^2 + 4x^2/s)\big)}{(2r_v^2 + 4x^2/s)^{3/2}}. \tag{5.3}$$

This formula makes it plain that h_s depends on space through $(x/\sqrt{s}, y)$, is antisymmetric about the x-axis, and is maximised along the curves $y = \pm\sqrt{r_v^2 + 2x^2/s}$. Decay as $|\boldsymbol{x}| \to \infty$ is slowest along these curves and proportional to x^{-1}.

We illustrate (5.3) and assess its range of validity by comparing it with MA for two sets of parameters in figure 6. The match is very good for $s = 10$ and $U_m = 0.4$ m s^{-1} (figures 6a,b), corresponding to $\gamma = 0.112$. It is less good for $s = 40$ and $U_m = 0.8$ m s^{-1} (figures 6c,d), unsurprisingly since $\gamma = 0.447$ is not particularly small and the MA prediction is obviously far from linear, with a pronounced asymmetry. The curves $y = \pm\sqrt{r_v^2 + 2x^2/s}$ shown in the figure are useful indicators of the structure of h_s for small enough γ.

https://doi.org/10.1017/jfm.2023.686 Published online by Cambridge University Press

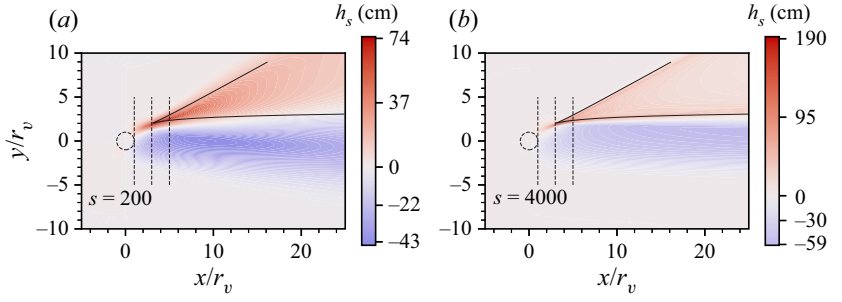


Figure 7. Caustics for swell impinging on a Gaussian vortex: the caustics (D6) (solid lines) are superimposed onto the MA prediction of h_s for $U_m = 0.8$ m s^{-1} and the indicated values of s. The dashed vertical lines correspond to the values $x = r_v$, $3r_v$ and $5r_v$ used in figure 8.

5.2. *Caustic regime:* $\gamma \gg 1$

The limit $\gamma \to \infty$ corresponds to an incident wave field that is almost a plane wave. It is natural to rescale variables according to $\Theta \mapsto \gamma\Theta$ and $X \mapsto \gamma^{-1}X$ so that (3.22) becomes

$$\mathcal{A}(X, y, K, \Theta) = \mathcal{A}_\star\,(K, \gamma\,\mathcal{S}(X, y, \Theta))\,, \tag{5.4}$$

where

$$\mathcal{S}(X, y, \Theta) \stackrel{\text{def}}{=} \Theta - \Delta(y - X\Theta). \tag{5.5}$$

In (X, y, Θ)-space, the K-integrated action is concentrated in a thin $O(\gamma^{-1})$ layer around the surface $\mathcal{S}(X, y, \Theta) = 0$. Quantities such as H_s obtained by integrating the action with respect to Θ can be obtained by approximating the dependence of the right-hand side of (5.4) on $\mathcal{S}$ by $\delta(\mathcal{S})$. This fails, however, when (X, y, Θ) satisfy both

$$\mathcal{S}(X, y, \Theta) = 0 \quad \text{and} \quad \partial_\Theta \mathcal{S}(X, y, \Theta) = 1 + X\,\Delta'(y - X\Theta) = 0. \tag{5.6a,b}$$

The corresponding curves in the (X, y)-plane are caustics near which $\int \mathcal{A}(X, y, K, \Theta)\,\mathrm{d}K\,\mathrm{d}\Theta$ is an order $\gamma^{1/2}$ larger than elsewhere; correspondingly, $H_s = O(\gamma^{1/4})$. In figure 7, the two caustics meet at a cusp point from opposite sides of a common tangent. The cusp point is located by the condition $\partial^2_\Theta \mathcal{S} = 0$, and the integrated action at the cusp point is $O(\gamma^{2/3})$ so that $H_s = O(\gamma^{1/3})$. We have verified numerically these γ scalings at the caustics and at the cusp point by varying s in the MA solutions.

For the Gaussian vortex (4.1), the system (5.6*a*,*b*) can be solved to obtain an explicit equation for the caustics. This equation is derived in Appendix D and given by (D6). It describes two curves $y(x)$ emanating from the cusp point at $x = x_c$ given by (D5). The caustics (which depend on U_m but not on s) are indicated in figures 3(*b*,*d*,*f*,*h*). For the parameters of the figure, the caustics do not map regions of particularly large h_s. This is unsurprising since γ is at most 0.447.

To assess how large γ, or equivalently s, needs to be for caustics to be the dominant feature of H_s, in figure 7 we show h_s computed from MA for $U_m = 0.8$ m s^{-1} and $s = 200$ ($\gamma = 1$, figure 7*a*) and $s = 4000$ ($\gamma = 4.47$, figure 7*b*). It is only for $s = 4000$ that the caustics are evidently controlling the significant wave height pattern. We emphasise that $s = 200$ and *a fortiori* $s = 4000$ are unrealistically large values: observational estimates for s in the open ocean seldom exceed $s = 80$. We conclude that caustics are unlikely to play a role in real ocean conditions.

With academic rather than practical interest in mind, then, we show in figure 8 the integrated action $\int \mathcal{A}\,\mathrm{d}k$ as a function of y for three different values of x (identified by

https://doi.org/10.1017/jfm.2023.686 Published online by Cambridge University Press

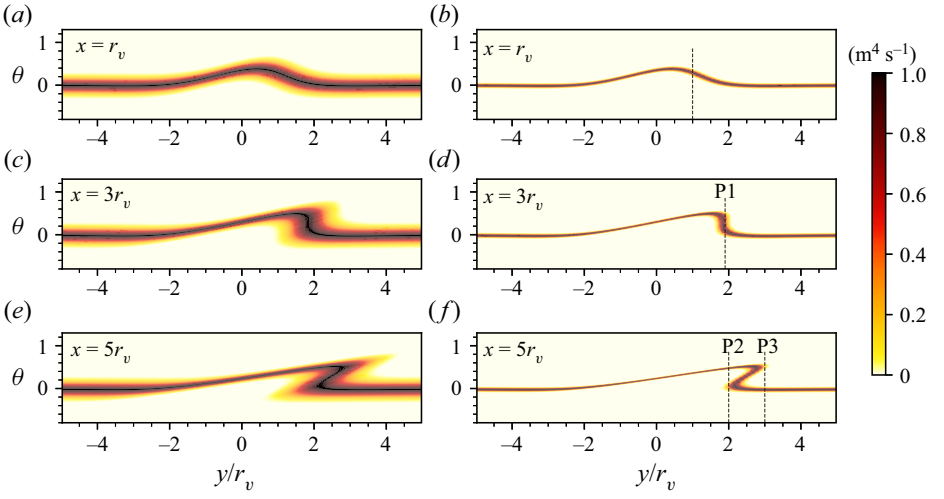


Figure 8. Wavenumber-integrated action density $\int \mathcal{A}(x, y, k, \theta)\, \mathrm{d}k$ as a function of y and θ for $x = r_v, 3r_v, 5r_v$ corresponding to the significant wave height shown in figure 7 for (a,c,e) $s = 200$ and (b,d,f) $s = 4000$. Line P1 in (d) corresponds to the values of (x, y) of the cusp from where the caustics emanate; P2 and P3 are associated with points on each of the two caustics.

dashed vertical lines in figure 7). The figure illustrates how caustics emerge from a fold singularity in the surface $\mathcal{S}(x, y, \theta) = 0$ along which action is concentrated in the (x, y, θ) phase space. For $x = r_v$, the surface is a graph over (x, y), and there are no caustics; for $x = x_c \approx 3r_v$, the surface has a single point of vertical tangency (P1 in figure 8f) corresponding to the birth of caustics at a cusp in the (x, y)-plane; for $x = 5r_c$, there are two points of vertical tangency, P2 and P3 in figure 8(h), corresponding to the two caustic curves. The picture is increasingly blurred as s decreases (compare figures 8(a,c,e) with figures 8(b,d,f) and with figure 2), explaining the diminishing importance of caustics for H_s.

6. Discussion and conclusion

The main results in this study are obtained by approximate solution of the wave-action equation in the four-dimensional position–wavenumber space. The organizing principle identified by the analysis is that scattering of SGWs by spatially compact currents results in the deflection function $\Delta(y)$ in (3.17). Although Δ varies linearly with the vertical vorticity of the currents, it figures in a nonlinear transformation of the action density. This nonlinear transformation produces the modulation of the significant wave height H_s behind the scattering region, e.g. the expression for H_s in (3.29). Quantities that depend on other moments (e.g. Stokes drift) behave similarly and could be inferred readily from our explicit forms (3.15) and (3.22) for the wave-action density.

While we have obtained these results for deep-water SGWs, they apply essentially unchanged to other two-dimensional waves with isotropic dispersion relation such as finite-depth SGWs or Poincaré waves. The conclusions that we draw about H_s can also be rephrased in terms of other root-mean-square quantities relevant to waves other than SGWs. With a little effort, the approach that we adopt, based on the matched asymptotics treatment of the wave-action equation, could be extended further to three-dimensional waves and to anisotropic dispersion relations. Our results could be extended easily to

https://doi.org/10.1017/jfm.2023.686 Published online by Cambridge University Press

account for vertically sheared currents using the modified dispersion relation of Kirby & Chen (1989) (which involves a Doppler shift term that is nonlinear in $\boldsymbol{k}$).

In addition to the WKB approximation used to derive the action conservation equation (2.1), there are two independent approximations involved:

(*a*) the current speed is much less than the group velocity of the incident swell;
(*b*) swell with small directional spreading is incident on a region of spatially compact currents, e.g. an axisymmetric vortex or a vortex dipole.

Provided that (*a*) and (*b*) are satisfied, the approximate solution of the wave-action equation compares well with numerical solutions provided by WW3.

Approximation (*a*) is usually justified. To challenge (*a*), one must consider current speeds such as 2 m s^{-1}, e.g. observed as a peak current speed in the Agulhas system (Quilfen & Chapron 2019). Swell with 100 m wavelength has group velocity $\sim$6 m s^{-1}, so the small parameter in (*a*) is as large as 1/3. In less extreme cases, approximation (*a*) will be satisfied.

Approximation (*b*) is less secure: ocean swell is not sufficiently unidirectional to strongly justify (*b*) – e.g. see the δ column in table 1. Over long distances, the continuous scattering by uncorrelated currents leads to a broadening of the angular spectrum. When approximation (*a*) applies, this broadening is described by the directional diffusion equation for wave action derived by Villas Bôas & Young (2020). This diffusion process is one of the mechanisms that makes swell with very small values of δ unlikely. However, our computations for a Gaussian vortex indicate that our asymptotic results are reliable for the moderately small values of δ typical of swell.

Because of the relatively large directional spreading of ocean swell, the mathematical ideal of a sharp wave caustic is not realised. Instead, the caustic singularity is 'washed out' (Heller *et al.* 2008). Behind a vortex, we find instead an elongated streaky pattern in H_s.

Our results show that H_s behind an axisymmetric vortex with parameters in table 1 has spatial variation as large as $\pm 30\,\%$ of the incident constant value $H_{s\star}$. Spatial inhomogeneities in H_s of this magnitude are important for wave breaking and exchange of momentum, heat and gas between the ocean and atmosphere. For example, airborne observations of the ocean surface by Romero *et al.* (2017) indicate that $\pm 30\,\%$ variations in H_s are associated with an order of magnitude increase in whitecap coverage.

The directional diffusion equation of Villas Bôas & Young (2020) uses only approximation (*a*). One does not need to assume that the wave field is strongly unidirectional or that the currents are spatially compact. Moreover, the directional diffusion equation is obtained without detailed consideration of the perturbations to the action spectrum that accompany wave scattering. But there is useful information hiding in these unexamined perturbations to the action spectrum. We are engaged currently in extracting these perturbations, calculating the attendant spatial variability to H_s, and relating the statistics of these fluctuations in H_s to those of the surface currents. These future developments promise to explain numerical experiments that identify relations between the spectral slopes of surface-current spectra and those of significant wave height (Villas Boâs *et al.* 2020).

Supplementary material. Computational Notebook files are available as supplementary material at https://doi.org/10.1017/jfm.2023.686 and online at https://www.cambridge.org/S0022112023006869/JFM-Notebooks/files/Figure-3.ipynb.

Acknowledgements. We thank V. Shrira for conversations about this work.

https://doi.org/10.1017/jfm.2023.686 Published online by Cambridge University Press

Funding. J.V. and H.W. are supported by the UK Natural Environment Research Council (grant NE/W002876/1). A.B.V.B. is supported by NASA award 80NSSC23K0979 through the International Ocean Vector Winds Science Team. W.R.Y. is supported by the National Science Foundation award 2048583.

Declaration of interests. The authors report no conflict of interest.

Data availability statement. The WW3 configuration files applied in this work can be found at https://github.com/biavillasboas/SwellVortex.

Author ORCIDs.
Han Wang https://orcid.org/0000-0002-5841-5474;
Ana B. Villas Bôas https://orcid.org/0000-0001-6767-6556;
William R. Young https://orcid.org/0000-0002-1842-3197;
Jacques Vanneste https://orcid.org/0000-0002-0319-589X.

Appendix A. Incident spectrum

We use the separable spectrum

$$\mathcal{F}_\star(k,\theta) = \zeta_{rms\star}^2\, F_\star(k)\, D_\star(\theta). \tag{A1}$$

The wavenumber function in (A1) is

$$F_\star(k) \overset{\text{def}}{=} \frac{2}{\operatorname{erfc}(-\sigma_\star/\sqrt{2}\,\delta_\sigma)} \frac{\exp(-(\sigma-\sigma_\star)^2/2\delta_\sigma^2)}{\sqrt{2\pi\delta_\sigma^2}} \frac{1}{k}\frac{\mathrm{d}\sigma}{\mathrm{d}k}, \tag{A2}$$

where erfc is the complementary error function. It corresponds to a Gaussian spectrum in frequency truncated at $\sigma = 0$. The angular part of the spectrum in (A1) is

$$D_\star(\theta) \overset{\text{def}}{=} \frac{\Gamma(s+1)}{2\sqrt{\pi}\,\Gamma(s+\frac{1}{2})} \cos^{2s}\left(\frac{\theta}{2}\right) \tag{A3}$$

(Longuet-Higgins *et al.* 1963), which corresponds to incoming waves spread around $\theta = 0$. The four parameters in this model spectrum are the root-mean-square sea-surface displacement $\zeta_{rms\star}$, the peak radian frequency $\sigma_\star = \sqrt{gk_\star}$, the spectral width δ_σ, and the directional spreading parameter s. Normalisation is ensured with

$$\int_{-\pi}^{\pi} D_\star(\theta)\,\mathrm{d}\theta = 1 \quad \text{and} \quad \int_0^\infty F_\star(k)\,k\,\mathrm{d}k = 1. \tag{A4a,b}$$

In the narrow-band limit $\delta_\sigma/\sigma_\star \ll 1$ and $s \gg 1$, the spectrum is approximated by (2.6) with $\delta_k = 2\delta_\sigma\sqrt{k_\star/g}$ and $\delta_\theta = \sqrt{2/s}$. The parameter δ_θ captures the standard deviation in the angular distribution, which is the definition of 'directional spreading' (Kuik, Van Vledder & Holthuijsen 1988). We note that the expressions for directional spreading are sometimes formally different, but equivalent to our expression for δ_θ at large s. For example, another popular way to state the definition for a generic directional distribution

https://doi.org/10.1017/jfm.2023.686 Published online by Cambridge University Press

is

$$\sigma_\theta \overset{\text{def}}{=} \left[2\left(1-(a^2+b^2)^{1/2}\right)\right]^{1/2}, \tag{A5}$$

where

$$a = \int \cos\theta\, D_\star(\theta)\,\mathrm{d}\theta \quad \text{and} \quad b = \int \sin\theta\, D_\star(\theta)\,\mathrm{d}\theta \tag{A6a,b}$$

(Villas Boâs *et al.* 2020). Using the expression for $D_\star$ in (2.6), we can compute the integrals in (A6*a*,*b*) analytically, getting $a = \mathrm{e}^{-1/s}$ and $b = 0$. Therefore,

$$\sigma_\theta^2 = 2(1-\mathrm{e}^{-1/s}) \to 2/s \quad \text{as } s \to \infty. \tag{A7}$$

Thus the definition of σ_θ in (A5) indeed agrees with the parameter δ_θ at large s.

Appendix B. Set-up of WAVEWATCH III

We compare our results with numerical simulations from an idealised set-up of WW3 that integrates the action balance equation (2.1). Here, we focus on freely propagating swell-type waves, so the effects of wind forcing, nonlinear interactions and wave breaking are ignored (e.g. Villas Boâs *et al.* 2020). We use WW3 version v6.07.1 (https://github.com/NOAA-EMC/WW3/releases/tag/6.07.1) to solve (2.1) on a 1000 km × 1000 km Cartesian domain with 5 km grid spacing. To resolve swells with $s = 10$ and 40, the spectral grid has 80 directions and 32 frequencies. Larger values of s (i.e. narrower directional spreading) would require higher directional resolution for the model to converge. We use the global integration time step 200 s, spatial advection time step 50 s, spectral advection time step 12 s, and minimum source term time step 5 s. We verified that decreasing the time stepping or the spatial grid spacing does not significantly change the results (not shown).

All simulations are initialised with the narrow-banded wave spectrum in (A1). Waves enter the domain from the left boundary with initial mean direction $\theta = 0^\circ$ (propagating from left to right), directional spreading parameter $s = 10$ or $s = 10$, peak frequency $\sigma_\star = 0.61\text{rad s}^{-1}$ (peak period 10.3 s), spectral width $\delta_\sigma = 0.04$, and $H_{s\star} = 1$ m. The boundary condition at the left boundary is kept constant throughout the experiment, and each experiment is run until steady state is reached.

As mentioned in § 4.1, a control run is conducted in the absence of currents. Although there is no scattering from the currents, a non-uniform $h_s^{ctrl} = H_s^{ctrl} - H_{s\star}$ arises, due to the limited domain size in y, which leads to a reduction of incident wave action from waves arriving from large $|y|$ – an effect that is more pronounced at large x. As s increases, the action density in the incident spectrum is more concentrated in the x-direction, leading to less leakage of wave action through the top and bottom boundaries, and a more spatially uniform h_s^{ctrl}. This leakage of wave action corresponds to a reduction of 5 % in h_s^{ctrl} for $s = 10$, and 2 % for $s = 40$ towards the right-hand side boundary.

Appendix C. MA–WW3 mismatch in the scattering region

We develop a heuristic correction to MA that we show captures the non-zero h_s in the scattering region. First, we note that the non-zero h_s in the scattering region from WW3 appears localised, likely caused by the term proportional to $\partial_k \mathcal{A}$ in (3.9), as the terms proportional to $\partial_\theta \mathcal{A}$ result in non-local effects. This observation is confirmed by a WW3 run, which we refer to as WW3$^-$, where the term in $\partial_k \mathcal{A}$ is suppressed in the wave-action

https://doi.org/10.1017/jfm.2023.686 Published online by Cambridge University Press

equation, yielding a more uniform h_s in the scattering region (see figure 9*d*). We then recall that in the MA solution, the insignificance of the $\partial_k \mathcal{A}$ term is due to the approximation of a single dominant wavenumber in the steps leading to (3.24). We thus return to the approximation (3.12) of the wave-action transport equation in the scattering region and relax the approximation of replacing k by $k_\star$. We focus on the θ-integrated action

$$\mathcal{B}(\boldsymbol{x}, k) = \int \mathcal{A}(\boldsymbol{x}, \boldsymbol{k})\, \mathrm{d}\theta, \tag{C1}$$

which satisfies

$$c(k)\, \partial_x \mathcal{B} - U_x(\boldsymbol{x})\, k\, \partial_k \mathcal{B} = 0. \tag{C2}$$

Noting that $c(k) = g^{1/2} k^{-1/2}/2$, we solve this equation using the method of characteristics to find

$$\mathcal{B}(\boldsymbol{x}, k) = \mathcal{B}_\star\big(\big(k^{-1/2} - g^{-1/2}\, U(\boldsymbol{x})\big)^{-2}\big). \tag{C3}$$

The significant wave height is deduced by integration as

$$H_s(\boldsymbol{x}) = \left(\frac{16}{g^{1/2}} \int \mathcal{B}_\star\big(\big(k^{-1/2} - g^{-1/2}\, U(\boldsymbol{x})\big)^{-2}\big) k^{3/2}\, \mathrm{d}k\right)^{1/2}. \tag{C4}$$

We now change the integration variable, taking advantage of the localisation of $\mathcal{B}_\star(k)$ to ignore the corresponding change in the lower limit of integration, and obtain

$$\begin{aligned} H_s(\boldsymbol{x}) &= \left(\frac{16}{g^{1/2}} \int \mathcal{B}_\star(k) (k^{-1/2} + g^{-1/2}\, U(\boldsymbol{x}))^{-6} k^{-3/2}\, \mathrm{d}k\right)^{1/2} \\ &= \left(\frac{16}{g^{1/2}} \int \mathcal{B}_\star(k)\, k^{3/2} (1 + k^{1/2} g^{-1/2}\, U(\boldsymbol{x}))^{-6}\, \mathrm{d}k\right)^{1/2} \\ &= \left(\frac{16}{g^{1/2}} \int \mathcal{B}_\star(k)\, k^{3/2} \left(1 + \frac{U(\boldsymbol{x})}{2\, c(k)}\right)^{-6} \mathrm{d}k\right)^{1/2}. \end{aligned} \tag{C5}$$

At this point, we can approximate $c(k)$ by $c_\star$ in the small $O(\varepsilon)$ term $U(\boldsymbol{x})/(2\, c(k))$ and use two binomial expansions to obtain

$$H_s(\boldsymbol{x}) \approx H_{s\star} \left(1 - \frac{3U(\boldsymbol{x})}{2c_\star}\right). \tag{C6}$$

We emphasise the heuristic nature of this approximation (MA$^+$), which is formally no more accurate than the MA approximation $H_s(\boldsymbol{x}) = H_{s\star}$ since it neglects some, though not all, $O(\delta)$ terms. Nonetheless, it captures most of the significant wave height anomaly close to the Gaussian vortex, as figure 9 demonstrates under parameters $s = 40$ and $U_m = 0.8\ \mathrm{ms}^{-1}$.

https://doi.org/10.1017/jfm.2023.686 Published online by Cambridge University Press

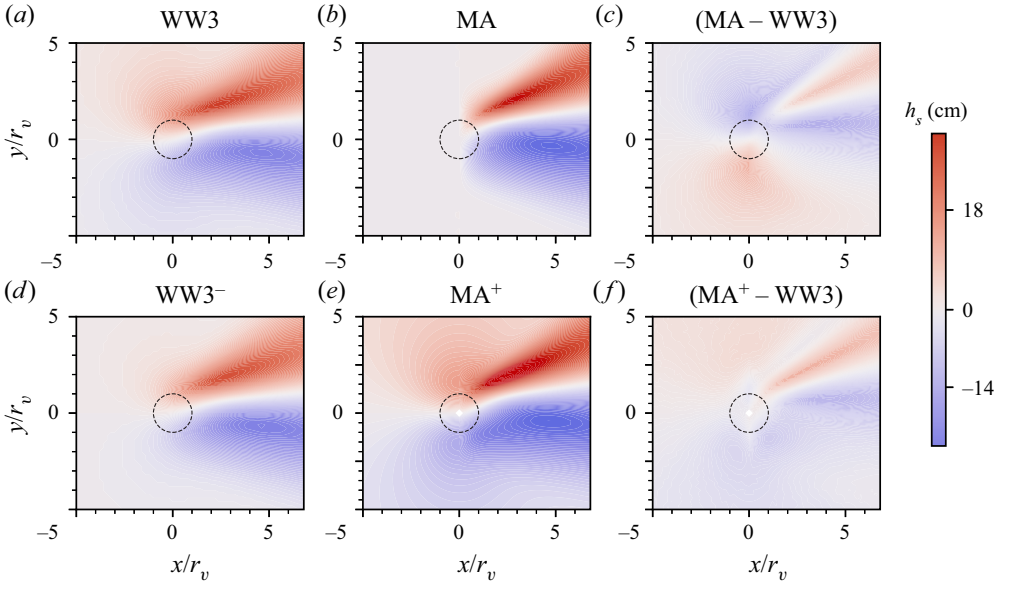


Figure 9. Significant wave height anomaly hs computed from (*a*) WW3, (*b*) MA (same as figures 3*g*,*h*), (*d*) WW3$^-$ (where the term proportional to $\partial_k \mathcal{A}$ is switched off) and (*e*) MA$^+$ as in (C6). Panels (*c*) and (*f*) show the differences between (*a*) and (*b*), and (*a*) and (*e*), respectively. All plots have the same colour bar.

Appendix D. Caustics for the Gaussian vortex

In the Gaussian vortex example, we can derive the locations of the caustics in the (x, y)-plane analytically. Using expression (4.3) for $\Delta(y)$, and introducing the functions

$$w(x, y) \overset{\text{def}}{=} -(y - x\theta)^2/r_v^2 \tag{D1}$$

and

$$q(x) \overset{\text{def}}{=} -2\pi r_v^4 c_\star^2/(x^2\kappa^2), \tag{D2}$$

we can write (5.6*a*,*b*) defining the caustics as

$$\theta - \frac{\kappa}{\sqrt{2\pi}\, r_v c_\star} \mathrm{e}^{w/2} = 0 \tag{D3}$$

and

$$w\,\mathrm{e}^w = q. \tag{D4}$$

Equation (D4) relates w to q, and takes the standard form defining the Lambert W-functions (see Olver 2010, (4.13.1)). This equation has two branches of solutions $w = W_i(q)$, $i = 0, -1$, when $0 < -q < \mathrm{e}$, and no solutions when $-q > \mathrm{e}$ ($q < 0$ by definition (D2)). The two branches meet at $q = -\mathrm{e}^{-1}$, which corresponds to

$$x = x_c \overset{\text{def}}{=} \sqrt{2\pi\mathrm{e}}\, r_v^2 c_\star/\kappa. \tag{D5}$$

Physically, the two branches $w = W_i(q)$ correspond to two caustic lines in the (x, y)-plane that emanate from a cusp point with $x = x_c$. The equation of the caustics is found using

https://doi.org/10.1017/jfm.2023.686 Published online by Cambridge University Press

(D1) and (D3) as

$$y = \frac{\kappa x \exp(W_i(q(x))/2)}{\sqrt{2\pi}\, r_v c_\star} + \sqrt{-W_i(q(x))}\, r_v, \quad x \geqslant x_c. \tag{D6}$$

The cusp point is at $(x, y) = (x_c, 2r_v)$.

The asymptotic form of the caustics for $x \to \infty$ is obtained readily by noting that $q(x) \to 0^-$ as $x \to \infty$, and then that $W_0(q) \to 0$ and $W_{-1}(q) \sim \ln(-q)$. Thus the $i = 0$ caustic asymptotes to a straight line, and the $i = -1$ caustic to $y \sim (2 \ln x)^{1/2}$.

References

Ardhuin, F., Gille, S.T., Menemenlis, D., Rocha, C.B., Rascle, N., Chapron, B., Gula, J. & Molemaker, J. 2017 Small-scale open ocean currents have large effects on wind wave heights. *J. Geophys. Res.: Oceans* **122** (6), 4500–4517.

Coste, C. & Lund, F. 1999 Scattering of dislocated wave fronts by vertical vorticity and the Aharonov–Bohm effect. II. Dispersive waves. *Phys. Rev.* E **60** (4), 4917.

Coste, C., Lund, F. & Umeki, M. 1999 Scattering of dislocated wave fronts by vertical vorticity and the Aharonov–Bohm effect. I. Shallow water. *Phys. Rev.* E **60** (4), 4908.

Dysthe, K.B. 2001 Refraction of gravity waves by weak current gradients. *J. Fluid Mech.* **442**, 157–159.

Dysthe, K., Krogstad, H.E. & Müller, P. 2008 Oceanic rogue waves. *Annu. Rev. Fluid Mech.* **40**, 287–310.

Ewans, K.C. 2002 Directional spreading in ocean swell. In *Ocean Wave Measurement and Analysis (2001)* (ed. B.L. Edge & J.M. Hemsley), pp. 517–529. American Society of Civil Engineers.

Gallet, B. & Young, W.R. 2014 Refraction of swell by surface currents. *J. Mar. Res.* **72** (2), 105–126.

Heller, E.J., Kaplan, L. & Dahlen, A. 2008 Refraction of a Gaussian seaway. *J. Geophys. Res.: Oceans* **113**, C09023.

Humbert, T., Aumaître, S. & Gallet, B. 2017 Wave-induced vortex recoil and nonlinear refraction. *Phys. Rev. Fluids* **2** (9), 094701.

Janssen, P. 2004 *The Interaction of Ocean Waves and Wind*. Cambridge University Press.

Kenyon, K.E. 1971 Wave refraction in ocean currents. *Deep-Sea Res.* **18**, 1023–1034.

Kirby, J.T. & Chen, T.-M. 1989 Surface waves on vertically sheared flows: approximate dispersion relations. *J. Geophys. Res.: Oceans* **94** (C1), 1013–1027.

Komen, G.J., Cavaleri, L., Donelan, M., Hasselmann, K., Hasselmann, S. & Janssen, P.A.E.M. 1996 *Dynamics and Modelling of Ocean Waves*. Cambridge University Press.

Kuik, A.J., Van Vledder, G.Ph. & Holthuijsen, L.H. 1988 A method for the routine analysis of pitch-and-roll buoy wave data. *J. Phys. Oceanogr.* **18** (7), 1020–1034.

Landau, L.D. & Lifshitz, E.M. 2013 *Fluid Mechanics: Course of Theoretical Physics*, vol. 6. Elsevier.

Longuet-Higgins, M.S., Cartwright, D.E. & Smith, N.D. 1963 Observations of the directional spectrum of sea waves using the motions of a floating buoy. In *Ocean Wave Spectra* (ed. E.C. Stephan), pp. 111–136. Prentice-Hall.

Mapp, G.R., Welch, C.S. & Munday, J.C. 1985 Wave refraction by warm core rings. *J. Geophys. Res.: Oceans* **90** (C4), 7153–7162.

McIntyre, M.E. 2019 Wave–vortex interactions, remote recoil, the Aharonov–Bohm effect and the Craik–Leibovich equation. *J. Fluid Mech.* **881**, 182–217.

Olver, F., Lozier, D., Boisvert, R. & Clark, C. (Eds) 2010 *NIST Handbook of Mathematical Functions*. Cambridge University Press.

Peregrine, D.H. 1976 Interaction of water waves and currents. *Adv. Appl. Mech.* **16**, 9–117.

Quilfen, Y. & Chapron, B. 2019 Ocean surface wave-current signatures from satellite altimeter measurements. *Geophys. Res. Lett.* **46** (1), 253–261.

Romero, L., Hypolite, D. & McWilliams, J.C. 2020 Submesoscale current effects on surface waves. *Ocean Model.* **153**, 101662.

Romero, L., Lenain, L. & Melville, W.K. 2017 Observations of surface wave–current interaction. *J. Phys. Oceanogr.* **47** (3), 615–632.

Villas Bôas, A.B., Cornuelle, B.D., Mazloff, M.R., Gille, S.T. & Ardhuin, F. 2020 Wave–current interactions at meso and submesoscales: insights from idealized numerical simulations. *J. Phys. Oceanogr.* **50** (12), 3483–3500.

https://doi.org/10.1017/jfm.2023.686 Published online by Cambridge University Press

VILLAS BÔAS, A.B. & PIZZO, N. 2021 The geometry, kinematics, and dynamics of the two-way coupling between wind, waves, and currents. U.S. CLIVAR Variations **19** (1), 18–26.

VILLAS BÔAS, A.B. & YOUNG, W.R. 2020 Directional diffusion of surface gravity wave action by ocean macroturbulence. *J. Fluid Mech.* **890**, R3.

VREĆICA, T., PIZZO, N. & LENAIN, L. 2022 Observations of strongly modulated surface wave and wave breaking statistics at a submesoscale front. *J. Phys. Oceanogr.* **52** (2), 289–304.

WHITE, B.S. & FORNBERG, B. 1998 On the chance of freak waves at sea. *J. Fluid Mech.* **355**, 113–138.

https://doi.org/10.1017/jfm.2023.686 Published online by Cambridge University Press